IEEE Access
Multidisciplinary ⋮ Rapid Review ⋮ Open Access Journal

Received 7 August 2022, accepted 28 August 2022, date of publication 1 September 2022, date of current version 12 September 2022.

*Digital Object Identifier 10.1109/ACCESS.2022.3203712*

RESEARCH ARTICLE

# Three-Phase Single-Carrier PWM Inverter for Isolated Grid-Tied PV Applications

**AHMED ISMAIL M. ALI[1], (Student Member, IEEE), MAHMOUD A. SAYED[1], (Senior Member, IEEE), TAKAHARU TAKESHITA[2], (Senior Member, IEEE), AND ZUHAIR MUHAMMED ALAAS[3], (Member, IEEE)**

[1]Department of Electrical Power and Machines Engineering, Faculty of Engineering, South Valley University, Qena 83523, Egypt
[2]Department of Electrical and Mechanical Engineering, Nagoya Institute of Technology, Nagoya 466-8555, Japan
[3]Electrical Engineering Department, Jazan University, Jazan 45142, Saudi Arabia

Corresponding authors: Ahmed Ismail M. Ali (a.ismail@eng.svu.edu.eg) and Mahmoud A. Sayed (mahmoud_sayed@ieee.org)

**ABSTRACT** Owing to their dependency of weather conditions, distributed generation systems are integrated with utility grid through power converters. This paper proposes an isolated three-phase based flyback-inverter (TBFBI) that can be used as a central-type inverter for grid-tied PV applications. To alleviate DC-current ripples at the input side, the proposed inverter utilizes only a single LC-filter with small passive elements size, which reduces the system footprint and cost. Mathematical modeling of the TBFBI in addition to its control technique is presented in detail. Compared with other differential based converters, the proposed control technique is designed considering the least number of control loops and required sensors by using terminal voltage estimation strategy. Continuous-modulation-scheme (CMS) combined with static-linearization strategy (SLS) is utilized to diminish the low-order odd harmonics. In addition, harmonic compensation technique is utilized to eliminate negative-sequence harmonic component (NSHC) from the grid-injected currents. Also, identical three single-phase high-frequency transformers (HFTs) are designed based-on ferrite and nanocrystalline cores to compare the inverter operating efficiency. The TBFBI is experimentally validated via laboratory prototype-based 200 V, 1.6 kW, and switching frequency of 50 kHz. Experimental results of 1.6 kW power flow show that THD of the grid current is 3.95%, peak-to-peak current ripple at the input DC-side is 2.1% of the average DC input current that matches the IEEE-1547 standards for grid-tied PV applications.

**INDEX TERMS** DC-AC grid-tied converter, flyback-inverter, high frequency transformer (HFT), harmonic compensation.

## I. INTRODUCTION

Renewable energy sources, such as photovoltaics, wind and fuel-cell energy generation systems, are wide-spreading over many countries, which encourage the power electronic converters evolution. Central-type inverter configurations offer a low cost solution for medium/high power grid-integrated solar PV systems [1], [2]. Despite the low MPPT efficiency of central-type PV architectures, central-type inverter configurations exhibit a lower-cost per kW in compared with the module, string, and multi-string inverter configurations due to their low manufacturing cost through the mass production [2], [3]. It worth to mention that central-type PV inverters may include non-isolated DC-DC converter for MPPT function [1], [4], [5]. However, the MPPT function can be implemented in the central-type isolated inverter without the need for non-isolated DC-DC converter in order to reduce system footprint and cost [6], [7], [8]. In this case, the MPPT controller decides the grid current reference signal that can be used to control the TBFBI. Many single-stage and multi-stages inverter structures have been presented in literature [9], [10], [11]. Non-isolated single/three-phase inverter

The associate editor coordinating the review of this manuscript and approving it for publication was Derek Abbott.

This work is licensed under a Creative Commons Attribution-NonCommercial-NoDerivatives 4.0 License.
For more information, see https://creativecommons.org/licenses/by-nc-nd/4.0/

architectures have been widely recommended [12], [13], which need an additional input boost converter stage to attain the required boosting of the input voltage [14]. Thus, it has two operation stages that complicates the converter controller and increases its cost. As well, most of these converter structures suffer from leakage current in different applications in addition to the requirement for isolating and voltage boosting transformers for high voltage applications, which increases the system losses, footprint, and cost [15], [16]. Consequently, transformer-based converter structures are presented by utilizing the line-frequency isolation transformer, which enlarges the system size and diminishes its efficiency. For efficiency enhancements and galvanic isolation requirements, high-frequency transformer (HFT) based inverter structures have been utilized instead of the line-frequency ones to reduce inverter footprint and enhance its efficiency [17]. Also, many modified inverter architectures have been presented for decoupling inductor/capacitor elimination [17], [18]. However, they mostly suffer from increased number of power components and passive elements, which rises implementation cost and reduces power density [19]. Motivated by multi-stage inverters drawbacks, single-stage inverter structures have been recommended in many applications for continuous DC input-current [6], [20], [21], [22], [23], [24], [25].

Differential-based inverter structures have been presented for different applications requirements. In [26], a switched capacitor differential boost-inverter and its control strategy was presented. The presented structure improves the static gain of the inverter without increasing the voltage stress over the power components, however, it incurs increased number of storage elements that implies higher controller order. In [27] and [28], a closed loop control technique with an optimized PI controller gain for non-ideal differential inverter was proposed in order to improve the controller behavior disturbance conditions. However, it has a high voltage stress over the converter elements that may affect the inverter efficiency profile. In [29], the theoretical values of the common and differential modes current ripples have been derived for modular multilevel dual-buck inverter, considering adjustable discontinuous modulation. However, it incurs many passive elements that increases system footprint and affect the power density. In [30], six-switch single-phase differential-based Cuk inverter was presented. However, it utilized increased switching devices that increases the system footprint and cost. In [31], the authors presented three-phase differentially flyback inverter considering three separated LC input filters at the input side for input current ripples minimization. In addition, a conventional PI-based grid-currents control loop is used for grid currents regulation [32]. In [33], the authors proposed three-phase SEPIC differential inverter for PV applications. However, the presented structure requires increased number of passive elements that enlarges converter size and footprint and increases its cost. In addition, owing to its large current ripples at the DC side terminals (about 90%), the presented structure requires large electrolytic capacitors at the DC input side in case of PV applications, which diminishes the system reliability and life-time. Electrolytic capacitors will also increase system footprint and cost. In addition, SEPIC based differential inverters should include identical three inductors and three HFTs, which is difficult to realize in practice, resulting in mismatch in module parameters. Therefore, the three-phase grid injected current waveforms with SEPIC based differential inverter includes high percentage of DC component resulting in unbalanced three-phase current waveform at the grid side. Therefore, the large DC electrolytic capacitor at the DC side in addition to the DC-components at the three-phase grid injected current diminish feasibility of the differential based SEPIC inverters for PV grid-tied applications.

Among the different buck-boost based inverter structures, flyback converters gained much of the researchers attention due to its simplicity and lower cost [1], [34]. In [1], an interleaved-flyback inverter is proposed for single-phase PV applications. However, it uses the transformers turn ratios for input-voltage boosting. Moreover, it uses parallel-components to enhance the inverter efficiency that rises the system cost and footprint. In [35], an iterative-learning down-sampled based controller is proposed for single-phase applications. The proposed controller realizes an acceptable overshoot and good steady-state response, however, it requires an unfolding H-bridge circuit. In [36], two-stage micro-inverter is presented for single-phase PV system for transformer utilization enhancement. However, it misses the galvanic isolation as well as the requirement for unfolding-circuit for DC-AC power conversion. In [34], a new hybrid BCM/DCM based control scheme is proposed for single-phase interleaved-flyback inverter to enhance its operating efficiency. However, it considers two-stage operation.

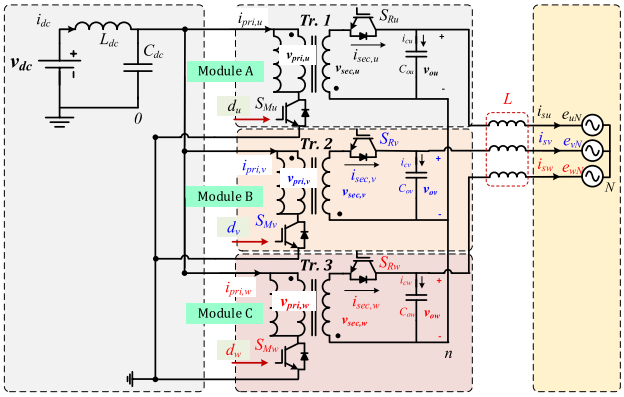


**FIGURE 1.** Three-Phase based flyback-inverter circuit structure.

This paper presents an isolated single-stage grid-tied TBFBI that can be used as a central-type PV inverter. The proposed TBFBI, shown in Fig. 1, comprises three flyback modules sharing the same DC input voltage and input LC filter. The proposed TBFBI introduces many features such as; low cost, high power-density, and simple control scheme. Also, it comprises reduced number of power switches and

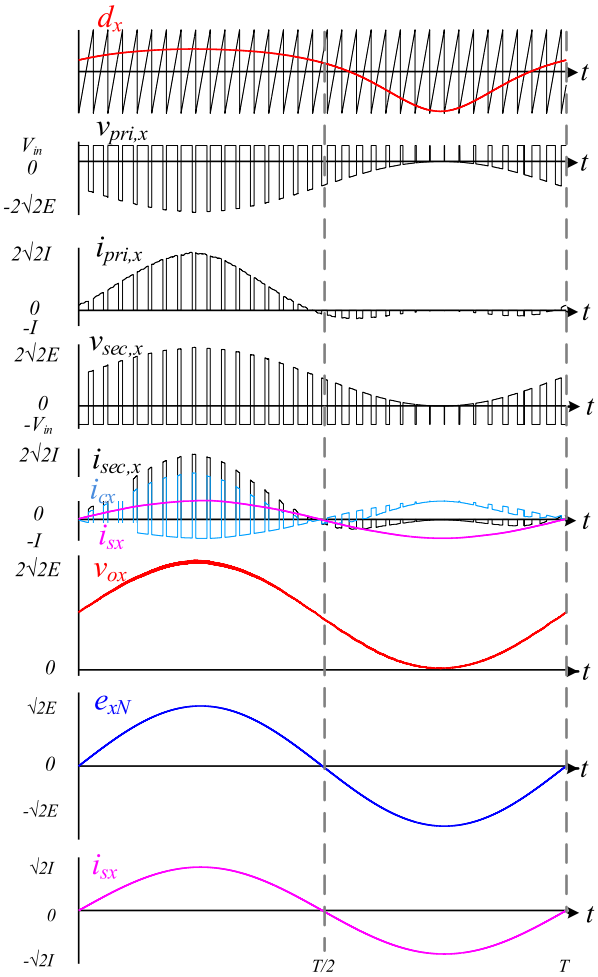


**FIGURE 2.** Proposed TBFBI PWM control strategy.

passive components with galvanic isolation property due to the HFT existence. Moreover, the turns ratio of HFT offers voltage boosting/bucking capability. Also, the proposed inverter offers a voltage step-up/step-down capability, which make it more attractive for isolated and non-isolated applications. In addition, TBFBI draws a ripple-free DC-input current that alleviates the capacitance over the PV-panel and improve the system reliability [23]. However, the temporarily operation of the proposed TBFBI results in a dc-bias through HFT primary winding, which may increase core loss and decrease the inverter efficiency [37]. Therefore, HFT-based nanocrystalline Core is designed in this paper to minimize the core loss and improve the system efficiency. In addition, a new mathematical model for the proposed TBFBI is presented in order to confirm the presence of the negative sequence low order harmonic components at the grid injected current waveforms, which need special control loop to be eliminated to meet the grid standard requirements. Also, the proposed TBFBI employs only a single LC filter at the input DC side providing the least passive elements count compared with other three-phase differential-based inverter structures that need individual LC filter at input DC side of each module. In addition, an improved control scheme for grid-injected current and terminal voltage regulation has been proposed for the single-stage TBFBI. Compared with the recently published control strategies of three-phase grid-tied counterpart topologies, the proposed control method uses the least number of control loops and required sensors, which simplifies the controller computational and execution time. Owing to the accurate estimation of TBFBI terminal voltage based on the mathematical model, the proposed control technique utilized only five sensors (i.e.; two voltage sensors and three current sensors) to detect grid voltages and currents. Also, the CMS combined with SLS is applied to control the TBFBI main and synchronous-switches for low-order harmonics mitigation. Moreover, due to the importance of the HFT in each module of the TBFBI from the efficiency point of view, a comparison between the ferrite and nanocrystalline cores for the TBFBI is presented. In addition, variations of all passive elements have been studied over wide-range of duty cycle for the passive elements selection of the proposed TBFBI based on the value, size, and stability issues, which affects system efficiency and power density. The proposed TBFBI is experimentally validated over system prototype based 200 V, 1.6 kW, 60 Hz, and switching-frequency of 50 kHz. The 50 kHz switching frequency is selected for ripples minimization and passive elements size reduction.

## II. PROPOSED GRID-TIED TBFBI

### A. CONFIGURATION AND OPERATION PRINCIPALS

The proposed TBFBI circuit configuration is depicted in Fig. 1, which consists of three flyback converter modules linked in parallel from the input DC-side and star-connected at the output-side. By considering a single compact LC-input filter, the TBFBI draw a ripple-free input DC current, which is essential for renewable energy applications such as; PV and fuel-cell [38]. For module (x) of the proposed TBFBI, Fig. 2 shows the module duty-cycle ($d_x$), voltage/current waveforms ($v_{\text{pri,x}}$, $i_{\text{pri,x}}$, $v_{\text{sec,x}}$, $i_{\text{sec,x}}$) of HFT input and output terminals, output-capacitor current ($i_{\text{cx}}$), and grid balanced voltage and current waveforms ($e_{\text{xN}}$, $i_{\text{sx}}$). Obviously, the proposed TBFBI operates over a wide duty-cycle variation range, which offers wide output AC voltage for different applications. In addition, the duty cycle of the proposed converter is derived considering a DC output voltage on the terminal of each module with a sinusoidal envelope. Therefore, duty cycle of each module shown in Fig. 2 is not a pure sinusoidal waveform to mitigate voltage stress on inverter components [6], [8], [23], [39]. Therefore, the modulation waveform consists of low-order harmonic and DC offset components enveloped with sinusoidal waveform to realize three-phase output voltage at the inverter output terminals. Derivation of duty cycle of each flyback module will be explained in details in the next section.

The operational modes of module-U of the proposed TBFBI are portrayed in Fig. 3, whereas its switching control signals are depicted in Fig. 4. It worth to mention that the

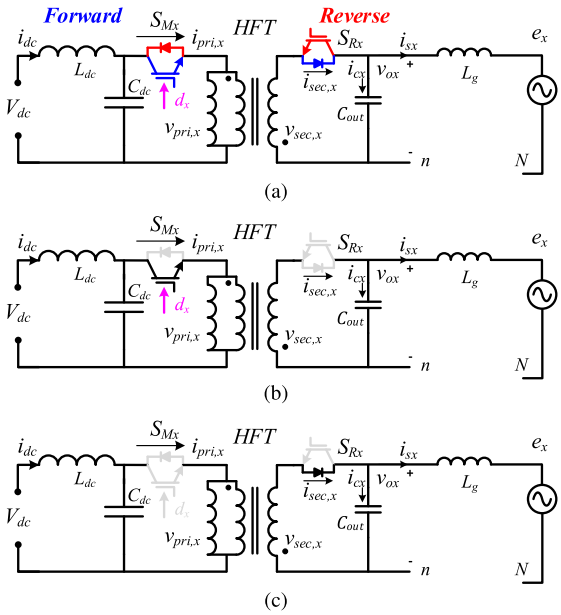


**FIGURE 3.** Temporarily power transfer in single-module of the TBFBI. (a) Bidirectional power flow of a single flyback module. (b) Stored Energy in the magnetizing inductance. (c) Released Energy from the magnetizing inductance.

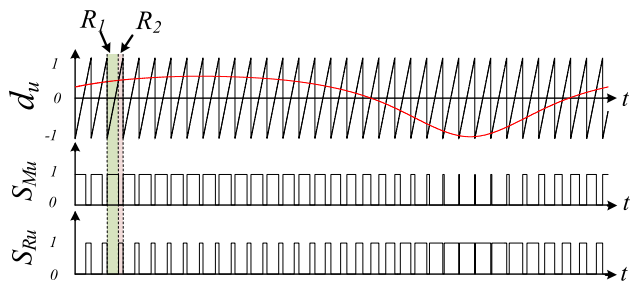


**FIGURE 4.** Gating signals generation of module-U of the TBFBI.

two switches of each flyback module are operating complementary considering CMS control strategy, as cleared in Fig. 3 and Fig. 4. The power streams from DC-side to grid during forward operational period, whereas it reverses during reversal operational period as depicted in Fig. 3(a). During forward operation, the main-switch and body-diode of synchronous-switch are sequentially ON and the power is injected to grid, where the switching waveforms are illustrated in time interval form zero to T/2 of Fig. 2. During reversal period, power flows into TBFBI module, which results in circulating power between the modules, as portrayed in time interval from T/2 to T of Fig. 2. The generation of PWM control signals of module-U is illustrated in Fig. 4. It worth to mention that the TBFBI is operating temporarily and power transfer occurs over storage element as shown in Fig. 3(b) and Fig. 3(c). Therefore, the HFT is utilized for two functions; 1) storage inductance, 2) galvanic isolation. Accordingly, during the ON-period of the main-switch, the input power is stored in the HFT magnetizing inductance $L_{\mathrm{Mx}}$ and grid current is supplied by the output capacitor of each module, see Fig. 3(b) and region ($R_1$) of Fig. 4. During the OFF-period of the main-switch, the stored energy in $L_{\mathrm{Mx}}$ is released through secondary side to supply grid current and charging the output capacitor as shown in Fig. 3(c). Similarly, during the ON-period of the synchronous-switch, the reverse power is stored in the HFT magnetizing inductance as cleared in region ($R_2$) of Fig. 4. During the OFF-period of the synchronous-switch, the stored energy is release in the reverse direction to the input DC supply. However, the duty cycle (i.e.; modulation waveform) of each flyback module is synthesized considering minimized voltage stress and low order harmonic mitigation.

### B. MODULATION SCHEME AND MATHEMATICAL MODELING OF THE PROPOSED TBFBI

Although sharing the same DC source, each module of the TBFBI is controlled by wide-range of variable duty-cycle shifted by 120°. The voltage conversion ratio of each flyback module of the proposed inverter, considering CMS technique, can be expressed as follows [39], [40];

$$M_x = \frac{v_{\mathrm{ox}}}{v_{\mathrm{dc}}} = \frac{d_x}{1 - d_x} \tag{1}$$

where; $v_{\mathrm{ox}}$ is flyback module output-voltage, $v_{\mathrm{dc}}$ is input DC-voltage, and $d_x$ is Module-x duty-cycle.

Also, the resistances of inductor, diode, and switch of each module limit the inverter voltage-gain. Table 1 lists the voltage/current stress over each component of the proposed TBFBI. Generally, the TBFBI operation is based on modulating each module by 120° phase shifted duty cycles ($d_u$, $d_v$, and $d_w$) to synthesize a time-varying output voltage ($v_{\mathrm{ou}}$, $v_{\mathrm{ov}}$, and $v_{\mathrm{ow}}$). Therefore, the three output voltages comprise two voltage components; the line frequency sinusoidal voltages shifted by 120° superimposed with a DC offset voltage. However, elimination of the DC components at the output terminals of each flyback module can be optimally realized if the grid side voltages are balanced.

The grid three-phase balanced voltages can be expressed as follows;

$$\begin{bmatrix} e_{\mathrm{uN}} \\ e_{\mathrm{vN}} \\ e_{\mathrm{wN}} \end{bmatrix} = \sqrt{\frac{2}{3}} E \begin{bmatrix} \sin(\omega t + \alpha) \\ \sin(\omega t + \alpha - 2\pi/3) \\ \sin(\omega t + \alpha + 2\pi/3) \end{bmatrix} \tag{2}$$

where; E is the RMS line voltage, $\omega$ is the grid angular frequency, $\alpha$ is an arbitrary angle. The three-phase balanced grid currents can be expressed as follows;

$$\begin{bmatrix} i_{su} \\ i_{sv} \\ i_{sw} \end{bmatrix} = I \cdot \begin{bmatrix} \sin(\omega t + \alpha) \\ \sin(\omega t + \alpha - 2\pi/3) \\ \sin(\omega t + \alpha + 2\pi/3) \end{bmatrix} \tag{3}$$

where; I is the peak value of grid injected current.

The output voltage and current waveforms of three-phase grid-tied inverters utilizing dc-dc converter modules generate low-order odd and even harmonic components. The odd harmonics are generated by input-output nonlinearity, whereas even harmonics are generated by mismatch between inverter modules [22]. Therefore, SLS is applied at the

**TABLE 1.** Voltage and current stresses.

| | |
|---|---|
| Input Current, $i_{\text{pri,x}}$ | $\frac{n.v_{\text{ox}}}{(1-d_x)R_{eq}}$ |
| HFT magnetizing current, $i_M$ | $\frac{n.v_{\text{ox}}}{(1-d_x)R_{eq}}$ |
| Main-switch voltage, $V_{\text{SM}}$ | $V_{in}+\frac{v_{\text{ox}}}{n}$ |
| Main-switch current, $I_{\text{SM}}$ | $\frac{n.v_{\text{ox}}}{(1-d_x)R_{eq}}$ |
| Synchronous-switch voltage, $V_{\text{SR}}$ | $v_{\text{ox}}$ |
| Synchronous-switch current, $I_{\text{SR}}$ | $\frac{v_{\text{ox}}}{(1-d_x)R_{eq}}$ |

fundamental-frequency to mitigate low-order odd harmonics [22]. On the other hand, low order even harmonics can be compensated by using an external compensation strategy. Continuous-modulation-scheme (CMS) combined with SLS is used to generate the switches duty cycles. Hence, each module generates a time-varying output voltage as sinusoidal waveform superimposed with a common-mode DC offset. The common-mode DC offset is decoupled due to the star-connection at the grid-side. Therefore, output voltage of each module can be formulated as follows;

$$v_{\text{ox}}(t) = M_x \cdot v_{\text{dc}} \tag{4}$$

where; x=u, v, or w, $M_x$ is the converter conversion ratio, and $v_{\text{dc}}$ is the input DC-voltage.

Also, all modules output voltages can be formulated as;

$$\begin{bmatrix} v_{\text{ou}}(t) \\ v_{\text{ov}}(t) \\ v_{\text{ow}}(t) \end{bmatrix} = \begin{bmatrix} M_u \\ M_v \\ M_w \end{bmatrix} \cdot v_{\text{dc}} \tag{5}$$

Based-on the sinusoidal envelope of the output-voltage, the conversion ratio can be formulated as follows;

$$M_x = M_{\text{x,dc}} + M_{\text{x,ac}} \cdot \begin{bmatrix} \sin(\omega t+\alpha) \\ \sin(\omega t+\alpha-2\pi/3) \\ \sin(\omega t+\alpha+2\pi/3) \end{bmatrix} \tag{6}$$

Based-on (1) and (6), the duty cycle can be formulated as follows;

$$d_x = \frac{M_{\text{x,dc}} + M_{\text{x,ac}}K_x}{1 + M_{\text{x,dc}} + M_{\text{x,ac}}K_x} \tag{7}$$

where;

$$K_x = \begin{bmatrix} \sin(\omega t+\alpha) \\ \sin(\omega t+\alpha-2\pi/3) \\ \sin(\omega t+\alpha+2\pi/3) \end{bmatrix}$$

By applying SLS for low-order harmonic mitigation, the DC output component ($M_{\text{x,dc}}$) is equal to the peak value of sinusoidal component ($M_{\text{x,ac}}$). Consequently, the duty cycle can be modified as follows;

$$d_x = \frac{M + M \cdot K_x}{1 + M + M \cdot K_x} \tag{8}$$

where; $x = a$, $b$ or $c$ and $M = M_{\text{x,dc}} = M_{\text{x,ac}}$.

Therefore, all modules output voltages can be formulated, by substituting (6) and (8) into (5), as follows;

$$\begin{bmatrix} v_{\text{ou}}(t) \\ v_{\text{ov}}(t) \\ v_{\text{ow}}(t) \end{bmatrix} = M \cdot v_{\text{dc}} \cdot \left(1 + \begin{bmatrix} \sin(\omega t+\alpha) \\ \sin(\omega t+\alpha-\frac{2\pi}{3}) \\ \sin(\omega t+\alpha+\frac{2\pi}{3}) \end{bmatrix}\right) \tag{9}$$

### C. TBFBI HARMONIC MODELING AND ANALYSIS

Based-on large signal model of flyback module, the input primary current ($i_{\text{pri,u}}$) can be expressed as follows;

$$i_{\text{pri,u}} = \frac{i_{su}}{1-d_u} = i_{su} \cdot (1 + M + MK_x) \tag{10}$$

Therefore, from (10);

$$\begin{bmatrix} \frac{1}{1-d_u} \\ \frac{1}{1-d_v} \\ \frac{1}{1-d_w} \end{bmatrix} = 1 + M + M \cdot \begin{bmatrix} \sin(\omega t+\alpha) \\ \sin(\omega t+\alpha-2\pi/3) \\ \sin(\omega t+\alpha+2\pi/3) \end{bmatrix} \tag{11}$$

To analyze its superimposed harmonics orders, the balanced grid-injected current can be expressed as;

$$\begin{bmatrix} i_{su} \\ i_{sv} \\ i_{sw} \end{bmatrix} = I_m \begin{bmatrix} \sin(\omega t+\alpha) \\ \sin(\omega t+\alpha-2\pi/3) \\ \sin(\omega t+\alpha-4\pi/3) \end{bmatrix} + I_H \begin{bmatrix} \sin n(\omega t+\alpha) \\ \sin n(\omega t+\alpha-2\pi/3) \\ \sin n(\omega t+\alpha-4\pi/3) \end{bmatrix} \tag{12}$$

where; ($I_H$) is the current harmonic component of order (n).

Based-on (11 and 12), the transformer primary current can be formulated as follows;

$$\begin{aligned} &\begin{bmatrix} i_{\text{pri,u}}(t) \\ i_{\text{pri,v}}(t) \\ i_{\text{pri,w}}(t) \end{bmatrix} \\ &= (1+M)I_m \begin{bmatrix} \sin(\omega t+\alpha) \\ \sin(\omega t+\alpha-2\pi/3) \\ \sin(\omega t+\alpha-4\pi/3) \end{bmatrix} \\ &\quad + (1+M)I_H \begin{bmatrix} \sin n(\omega t+\alpha) \\ \sin n(\omega t+\alpha-2\pi/3) \\ \sin n(\omega t+\alpha-4\pi/3) \end{bmatrix} \\ &\quad + \frac{MI_m}{2} \begin{bmatrix} 1-cos(2\omega t+\alpha) \\ \frac{-1}{2}-cos(2\omega t+\alpha-2\pi/3) \\ \frac{-1}{2}-cos(2\omega t+\alpha-4\pi/3) \end{bmatrix} \\ &\quad + \frac{MI_H}{2} \begin{bmatrix} \cos((1-n)\omega t+\alpha)-cos((1+n)\omega t+\alpha) \\ \cos((1-n)\omega t+\alpha-2\pi/3))-cos((1+n)\omega t+\alpha-2\pi/3)) \\ \cos((1-n)\omega t+\alpha-4\pi/3))-cos((1+n)\omega t+\alpha-4\pi/3)) \end{bmatrix} \end{aligned} \tag{13}$$

Assuming lossless TBFBI and $\alpha = 0$, the power at input and output terminals are equal, as follows;

$$\begin{aligned} P_{in} &= v_{\text{dc}} i_{\text{pri}} = V_{in}(i_{\text{pri,u}} + i_{\text{pri,v}} + i_{\text{pri,w}}) \\ &= v_{\text{dc}} I_H (1+M)\{\sin n(\omega t) + \sin n(\omega t - 2\pi/3) \\ &\quad + \sin n(\omega t - 4\pi/3)\} + \frac{v_{\text{dc}} I_H M}{2}\{\cos((1-n)\omega t) \\ &\quad + \cos((1-n)\omega t - 2\pi/3) + \cos((1-n)\omega t - 4\pi/3)\} \\ &\quad - \frac{v_{\text{dc}} I_H M}{2}\{\cos((1+n)\omega t) + \cos((1+n)\omega t - 2\pi/3) \\ &\quad + \cos((1+n)\omega t - 4\pi/3)\} \end{aligned} \tag{14}$$

The output power can be formulated as follows;

$$\begin{aligned} P_{out} = & -\frac{\sqrt{2}EI_m}{2}\{\cos(2\omega t)+\cos(2\omega t-2\pi/3) \\ & +\cos(2\omega t-4\pi/3)\}+\frac{\sqrt{2}EI_H}{2}\{\cos((1-n)\omega t) \\ & +\cos((1-n)\omega t-2\pi/3)+\cos((1-n)\omega t-4\pi/3)\} \\ & -\frac{\sqrt{2}EI_H}{2}\{\cos((1+n)\omega t)+\cos((1+n)\omega t-2\pi/3) \\ & +\cos((1+n)\omega t-4\pi/3)\} \end{aligned} \tag{15}$$

Therefore, the three-phase currents, given in (13), can be modified as follows;

$$\begin{aligned} \begin{bmatrix} i_{\text{pri,u}}(t) \\ i_{\text{pri,v}}(t) \\ i_{\text{pri,w}}(t) \end{bmatrix} = & (1+M)I_m \begin{bmatrix} \sin(\omega t) \\ \sin(\omega t-2\pi/3) \\ \sin(\omega t-4\pi/3) \end{bmatrix} \\ & +(1+M)I_H \begin{bmatrix} \sin(2\omega t) \\ \sin(2\omega t-4\pi/3) \\ \sin(2\omega t-2\pi/3) \end{bmatrix} \\ & +\frac{MI_m}{2}\begin{bmatrix} 1 \\ \frac{-1}{2} \\ \frac{-1}{2} \end{bmatrix} \\ & -\frac{MI_m}{2}\begin{bmatrix} \cos(2\omega t) \\ \cos(2\omega t-2\pi/3) \\ \cos(2\omega t-4\pi/3) \end{bmatrix} \\ & +\frac{MI_H}{2}\begin{bmatrix} \cos(-\omega t) \\ \cos(-\omega t-2\pi/3) \\ \cos(-\omega t-4\pi/3) \end{bmatrix} \\ & -\frac{MI_H}{2}\begin{bmatrix} \cos(3\omega t) \\ \cos(3\omega t-2\pi/3) \\ \cos(3\omega t-4\pi/3) \end{bmatrix} \end{aligned} \tag{16}$$

## III. PROPOSED TBFBI CONTROL STRATEGY

As mentioned previously, the TBFBI operates with a variable duty-cycle, which affects the system stability. Therefore, it is very important to check the system stability with all duty cycle range. Consequently, developing an adequate dynamic modeling of the TBFBI is important for stability issue. The TBFBI control-to-output dynamic model, with a single LC input filter, is expressed as follows [37], [41];

$$G_{\text{vdx}}(S)=\frac{v_{\text{ox}}(S)}{d_x(S)}=G_0\frac{b_0+b_1S+b_2S^2+b_3S^3}{a_0+a_1S+a_2S^2+a_3S^3} \tag{17}$$

where; $G_0$ is the DC-gain, ($b_0$-$b_3$) are constants decides the zeros locations, and ($a_1$-$a_3$) are the constants of poles locations.

### A. TBFBI DYNAMICS AND PARAMETERS SELECTION

Considering 1.6 kW power flow, the system parameters can be designed according to [40] as 133 $\mu$H for the HFT magnetizing inductance, 12.8 $\mu$F for the output capacitor, 500 $\mu$H and 10 $\mu$F for the input filter inductance and capacitance, respectively. Also, stability of TBFBI depends mainly on the parameters of the input filter, magnetizing inductance of HFT, and output capacitor at the grid-side. Therefore, system stability is investigated considering wide-range variation of designed values based-on the size of passive elements, voltage and current ripples, phase margin, bandwidth, and stability over the wide-range of duty-cycle variations. Fig. 5 shows the variation effect of duty cycle (d=0.1∼0.8), input filter inductance ($L_{in}$=150∼1000 $\mu$H), transformer magnetizing inductance ($L_M$=100∼500 $\mu$H), and output capacitor ($C_{\text{ox}}$ = 5 ∼15 $\mu$F). Increasing output capacitance, $C_{\text{ox}}$, moves the complex poles towards the origin point, which enhances the system resonance. However, it may increase system size and cost. In contrast; decreasing the output capacitance increases imaginary parts of complex poles, which increases output voltage oscillations. On the other hand, increasing the magnetizing inductance moves complex poles towards the real axis that enhances the system resonance, however, it moves the RHP zero towards the origin point that decreases the inverter bandwidth. Owing to the inverter compactness, cost, and stability issues, optimal parameters of the proposed TBFBI are listed in Table 2.

**TABLE 2. Inverter parameters.**

| | |
|---|---|
| Input DC-voltage, $v_{\text{dc}}$ | 100 V |
| Input filter, $L_{\text{dc}}$, $C_{\text{dc}}$ | 150 $\mu$H, 10 $\mu$F |
| Grid voltage (L.L), $e_{\text{xN}}$ | 200 V, 60 Hz |
| Grid filter, L | 4 mH |
| HFT Mag. inductance, $L_{\text{Mx}}$ | 115 $\mu$H |
| HFT Leak. inductance, $L_{\text{leakage}}$ | 2.25 $\mu$H |
| Switching frequency, $F_{\text{SW}}$ | 50 kHz |

### B. CLOSED-LOOP COMPENSATOR DESIGN

Rigid compensator design of TBFBI is a critical issue to improve system stability and bandwidth (BW). The TBFBI closed loop transfer function, according to the inverter general control loop transfer function presented in [40], is formulated as follows;

$$T(S)=G_{\text{vd}}(S)G_{\text{lg}}(S)G_c(S)G_{\text{PWM}}(S)H_s(S)G_{\text{SLB}}(S) \tag{18}$$

where; T(s) is open-loop transfer function, $G_{\text{vd}}(s)$ is control-to-output transfer function, $G_{\text{lg}}(s)$ is grid filter transfer function, $G_c(s)$ is proposed compensator transfer function, $G_{\text{PWM}}(s)$ is modulator transfer function, $H_s(s)$ is sensor transfer function, $G_{\text{SLB}}(s)$ is Static Linearization Block transfer function,

Based-on the inverter transfer function in (17) and (18), Type-II compensator is required to stabilize the system with an improved phase-margin and response [42], [43]. Therefore, the compensator transfer function can be formulated as follows [42];

$$G_c(S)=G_{c,0}\frac{(1+\frac{S}{\omega_{z,1}})}{(1+\frac{S}{\omega_{p,1}})(1+\frac{S}{\omega_{p,2}})} \tag{19}$$

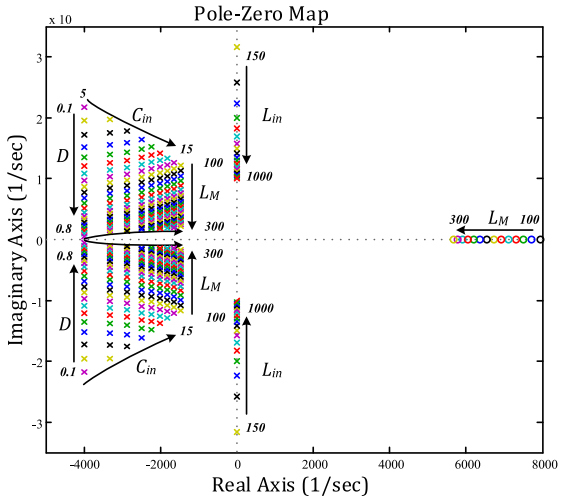


**FIGURE 5.** Effect of converter parameters variation on the location of dynamic poles and zero including the input filter.

where; $G_{c,0}$ is open-loop compensator gain, $\omega_{z,1}$,$\omega_{p,1}$ and $\omega_{p,2}$ are zeros and poles frequencies, respectively. In addition, the input LC filter has been designed at resonating frequency of $f_o$, which can be expressed as [40];

$$F_o = \frac{1}{2\pi\sqrt{L_{in}C_{in}}} \tag{20}$$

where the inverter resonating frequency must follow the expression;

$$10f_g \leq f_o \leq \frac{f_{SW}}{10} \tag{21}$$

Hence, $f_o$ is selected as 4 kHz. Hence, the input filter inductance and capacitance are designed as 150 $\mu$H and 10 $\mu$F, respectively. In addition, the grid inductance is selected as 4 mH [40].

The control scheme of the proposed inverter is portrayed in Fig. 6, which comprises of two control-loops:

- The main control-loop (Loop1), which regulates the grid-injected currents and output voltages of each converter module.
- The secondary control-loop (Loop2); which compensates negative sequence harmonics that distorts the grid current due to the inverter nonlinearities.

Based-on the harmonic modeling and analysis discussed in Section II-C, a Negative Sequence Harmonic Components (NSHC) are included in the grid currents. NSHC rotates in reverse direction with double frequency ($2\omega$) of the fundamental components, which is noticeable in the primary current envelope of each module. Therefore, a simple single-pole integrator is applied as a Selective Harmonic Elimination (SHE) strategy for NSHC compensation. In addition, the integrator in the second control-loop enrich the control system with an extra origin-pole. Therefore, the required compensator order is reduced from Type-II to conventional PI compensator, which simplifies the controller design and

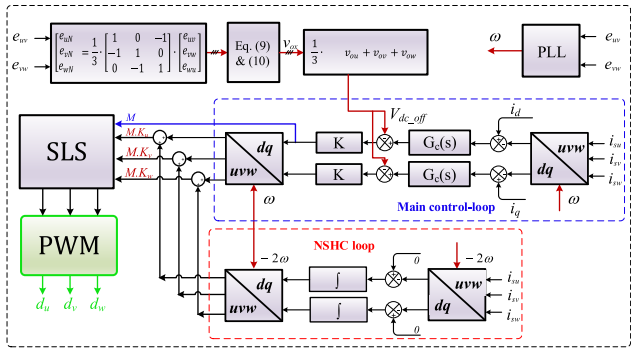


**FIGURE 6.** TBFBI closed-loop control-scheme.

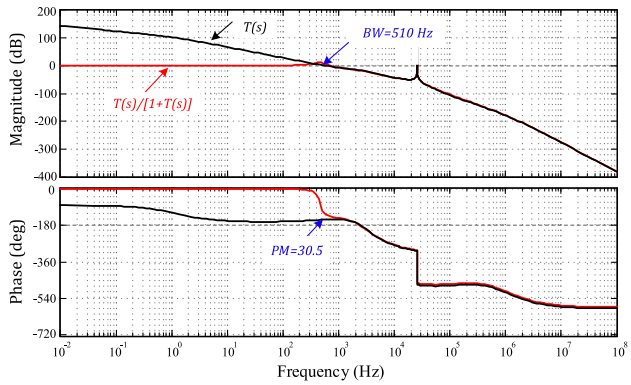


**FIGURE 7.** Closed-loop control-scheme bode plot of the proposed TBFBI using Type-II compensator.

reduces the computational time. The integrator extracts the second-order harmonics, which is compensated for sinusoidal grid-injected currents.

Also, Fig. 7 shows the bode plot of the TBFBI based-on the dynamic model and the compensator in (19). The compensator origin-pole increases closed-loop DC-gain of TBFBI inverter, which diminishes the mismatches among flyback converter modules to minimize circulating power between the modules. Also, it improves accuracy of the controller over wide-range variations of converter duty-cycle. According to Fig. 7, the DC-gain of the proposed inverter control system is 140 dB and the PM is 30.5°, which ensures system stability. Moreover, the inverter bandwidth is 510 Hz, which improves the inverter dynamics over a wide-range of duty cycle and frequency variations. In addition, the bode plot of the closed-loop controller including the second control-loop is shown in Fig. 8. Obviously, the integrator improved the PM to 39° and maintains high DC-gain due to its enriched origin pole. In addition, the system BW is increased to 700 Hz, which confirms the inverter stability over wide-range of frequency variations. Therefore, the proposed control system poses a major challenge by considering only two control loops without the need to incur complex control systems that needs long computational time and high controller specifications.

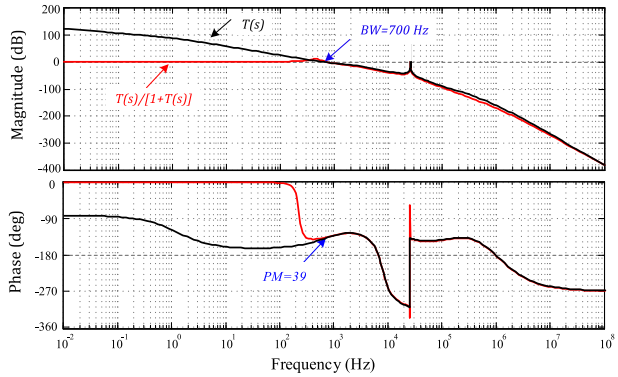


**FIGURE 8.** Closed-loop control-scheme bode plot of the proposed TBFBI with the two control-loops using PI controller.

**TABLE 3.** Simulation and experimental parameters.

| | |
|---|---|
| Rated inverter power, P | 1.6 kW |
| Input DC-voltage, $V_{dc}$ | 100 V |
| Input filter, $L_{dc}$, $C_{dc}$ | 151.14 $\mu$H, 10 $\mu$F |
| Input filter resistance, $r_{in}$ | 1.56 Ω |
| Grid voltage (L.L), E, $\omega$ | 200 V, 2×π× 60 rad/s |
| HFT Mag. inductance, $L_{Mx}$ | 115.85 $\mu$H |
| HFT primary resistance, $r_m$ | 50.34 mΩ |
| Output capacitor, $C_o$ | 10 $\mu$F |
| HFT inductance, $L_{leakage}$ | 2.26 $\mu$H |
| HFT turns ratio, n | 1:1 |
| Grid filter, $L_g$ | 4.06 mH |
| Grid inductor resistance, $r_g$ | 5.24 mΩ |
| Switching frequency, $F_{SW}$ | 50 kHz |
| PI controller gains, $K_P$,$K_I$ | 0.097 A/V, 280 rad. $sec^{-1}$ |

## IV. SYSTEM RESULTS

### A. SIMULATION RESULTS

The simulation findings of the proposed single-stage TBFBI are confirmed at rated converter power of 1.6 kW and under two operating conditions; without and with harmonic compensation technique. Fig. 9(a) and Fig. 9(b) show the system simulation results without and with NSHC compensation, respectively. In both cases, the three-phase grid voltages, grid currents, inverter output-voltages, DC input voltage, and DC input current are portrayed, respectively. Without compensation, the three-phase grid-currents are distorted with a high second-order harmonic component and the input DC current contains third-order harmonic. On the other side; the NSHC compensation strategy eliminates the low-order harmonic component and supply the grid with almost pure sinusoidal current waveforms. In addition, it minimizes the input DC current ripples to 2.1% that matches the IEEE-1547 harmonic standard for DER.

### B. EXPERIMENTAL SYSTEM CONFIGURATION

A laboratory prototype-based 200 V, 1.6 kW, 60 Hz grid frequency, and 50 kHz switching-frequency of the TBFBI is carried out to investigate the validity of the three-phase single-stage isolated TBFBI for grid-tied operation. It worth to mention that the dc side can be supplied by either PV modules or batteries due to the continuously smooth current

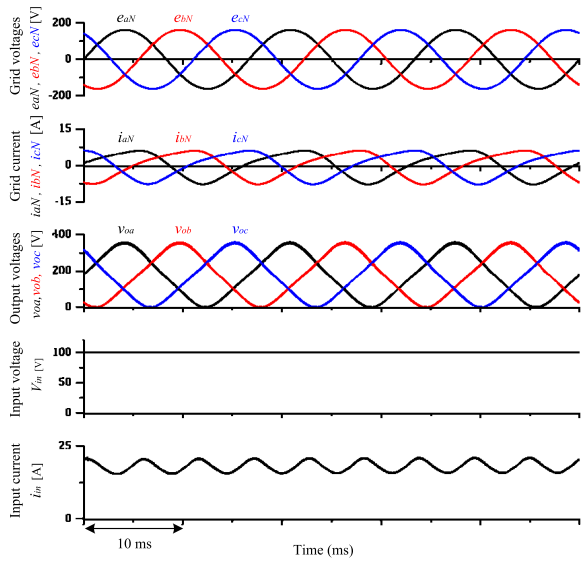


(a) Without NSHC compensation.

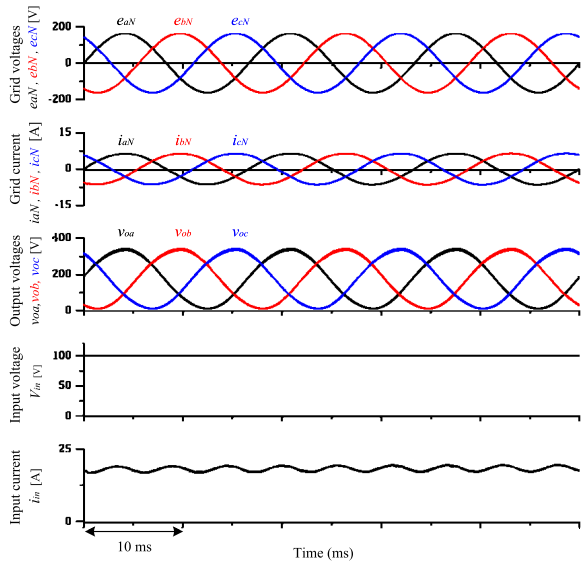


(b) With NSHC compensation.

**FIGURE 9.** DBFI simulation results.

at the dc side with small ripples. In this paper, a conventional dc source is considered at the dc side in order to confirm the system performance with the proposed control technique. However, future publication will consider PV module and its MPPT technique at the dc side by controlling only the two switches of each flyback module without any additional stages. Fig. 10 shows the system configuration and its control scheme. Also, experimental setup photograph is portrayed in Fig. 11, whereas all system parameters are listed in Table 3. The three-phase grid-currents and line-voltages are detected using LA55-P and LV25-P transducers, respectively. The phase-angle of the grid voltages is calculated from the grid line-voltages using phased-looked loop (PLL). Hence, the actual three-phase grid voltages and currents are converted to the dq-axis using abc/dq park transformation.

The error signal, obtained by comparing the reference and actual dq-axis grid currents, is fed to the PI controller for grid-current regulation, as illustrated in main control-loop of Fig. 6, and Fig. 10. Then, the output signals of the main control loop are summed with the output signals of the second loop, (i.e.; NSHC elimination loop) to obtain reference signals that can regulate the grid injected power at unity power factor and to realize three-phase sinusoidal grid current waveforms. The converter duty cycle can be calculated according to (8), which is compared with the high-frequency carrier signal to generate switching signals of the main and synchronous switches of each flyback module, as depicted in Fig. 4. The PCB dimension of each flyback module is 18*10 $cm^2$. The TBFBI is investigated for grid-tied operation at two modes; without NSHC-compensation (Mode-1), and with NSHC- compensation (Mode-2) and the grid current distortion is compared with standard permissible limits. The proportional and integral gains of the PI controller have been designed according to detailed analysis and explanation given in [21] and [22]. Based on the detailed mathematical model in section II, output voltage estimation of each module is used to reduce the required sensors, as shown in Fig. 6 and Fig. 10. Therefore, the proposed TBFBI uses only two voltage sensors and three current sensors at the grid-side, which is less than that used in other counterpart topologies. In addition, the system experimental waveforms are captured by 16-channel DL-850 Yokogawa digital oscilloscope. Moreover, system efficiency and THD have been measured and analyzed by WT1800 Yokogawa power analyzer. The digital controller PE-Expert 3, employing DSP TMS320C6713 board linked with MWPE3 Xilinx FPGA board (XC3S500E), is used to control the proposed system. The control algorithm is realized in the DSP board to calculate all switches duty cycles, transferred to the FPGA board to be compared with 50 kHz saw-tooth carrier signals to obtain gate signals of all switches.

### C. SINGLE-PHASE HFT DESIGN

Practically, commercial flyback-converters are available at low power ratings; (i.e; about 200 W). However, the proposed three-phase TBFBI is designed so that each flyback module transfers about 550 W to the grid-side. Performance of the proposed TBFBI depends mainly on the proper design of HFT in addition to passive elements. The design strategy can be summarized as follows [25];

- Considering low HFT leakage inductance for efficient operation.
- Using less turns number of high frequency windings. HFT windings are designed with 175(7 × 25)/0.20 Litz wire manufactured by USTC and its strand-diameter is less than 1/3 of strand skin-depth.
- Sandwiching of primary and secondary windings on one leg of the C-Core for better flux linkage as well as low fringing flux possibility.

According to the former study, the magnetizing inductance $L_M$ is designed to be 115 $\mu$H. HFT core is designed with

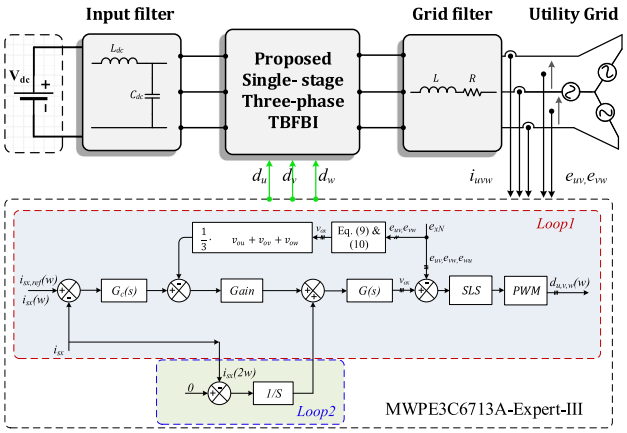


**FIGURE 10.** Experimental configuration of the proposed TBFBI with its control technique.

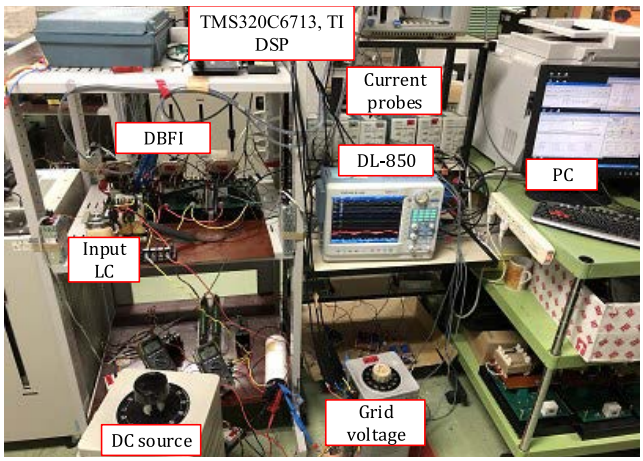


**FIGURE 11.** Proposed TBFBI photograph.

small-sized nanocrystalline C-Core considering 12 turns for primary and secondary windings (N), as shown in Fig. 12. Therefore, the air gap length is set to 1.45 mm based on the following formula;

$$l_e = \frac{N^2 \mu_0 A_{\text{core}}}{L_M} \tag{22}$$

where; $\mu_o$ is permeability of the free space and $l_e$ is the air gap length.

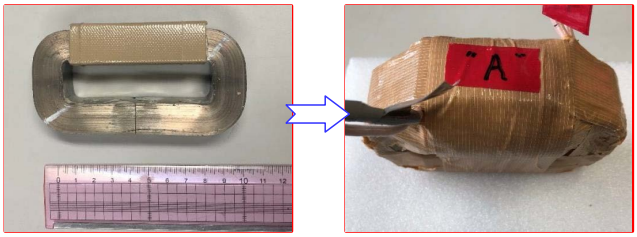

**FIGURE 12.** Nano-crystalline core-based HFT.

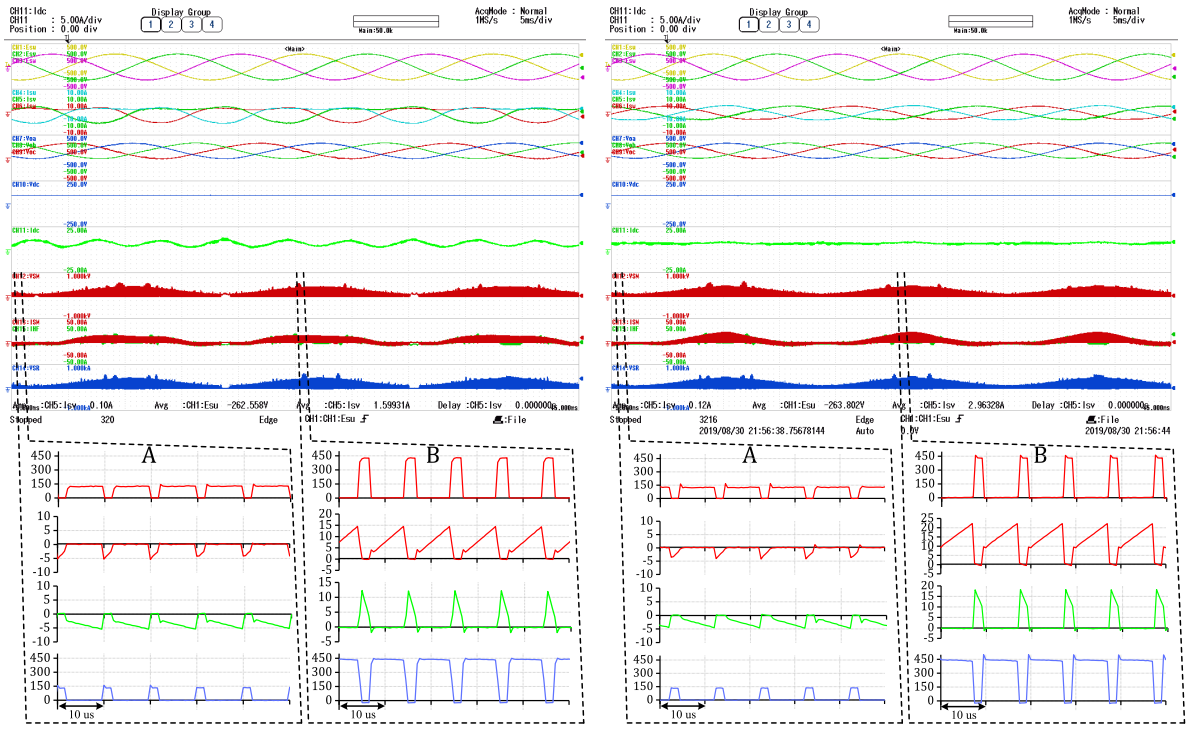


(a) Scope results for Mode-1.

(b) Scope results for Mode-2.

**FIGURE 13.** Experimental results of the proposed TBFBI at 0.8 kW.

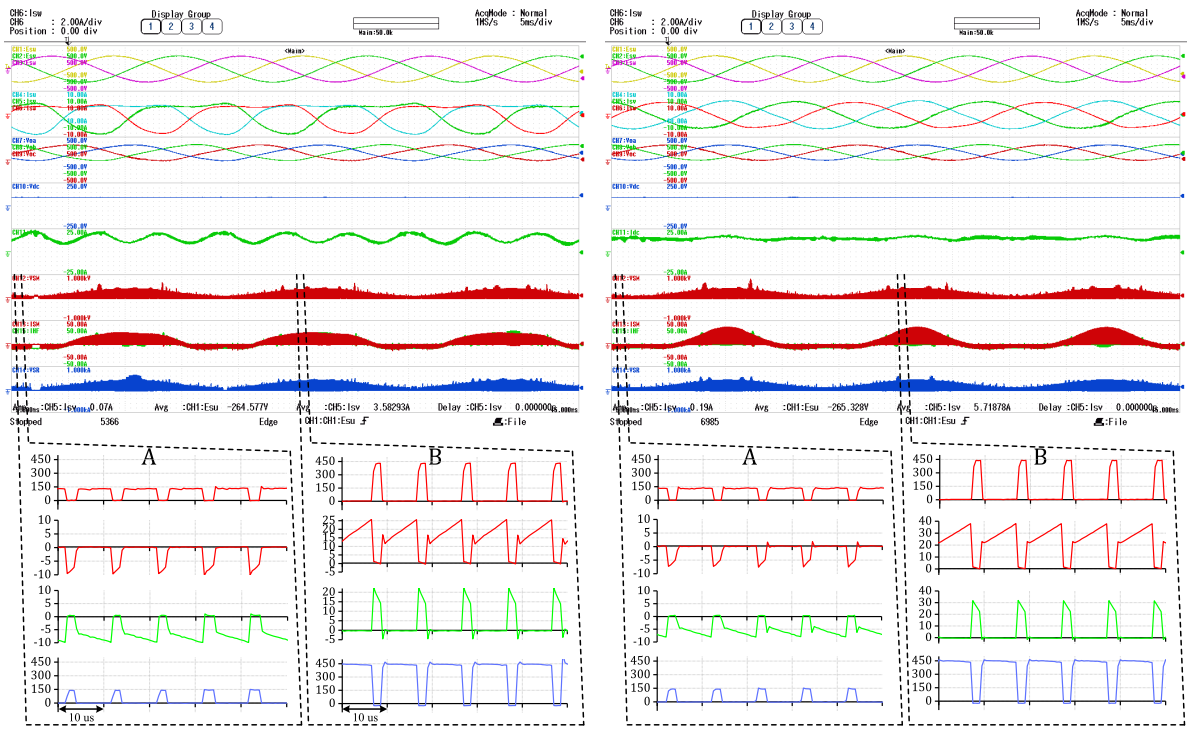


(a) Scope results for Mode-1.

(b) Scope results for Mode-2.

**FIGURE 14.** Experimental results of the proposed TBFBI at 1.6 kW.

### D. EXPERIMENTAL RESULTS

The experimental system has been carried out considering reference grid injected power of 0.8 kW and 1.6 kW considering Mode-1 and Mode-2. Fig. 13(a) and Fig. 13(b) shows the experimental results of the grid-tied TBFBI under Mode-1 and Mode-2, respectively at power flow

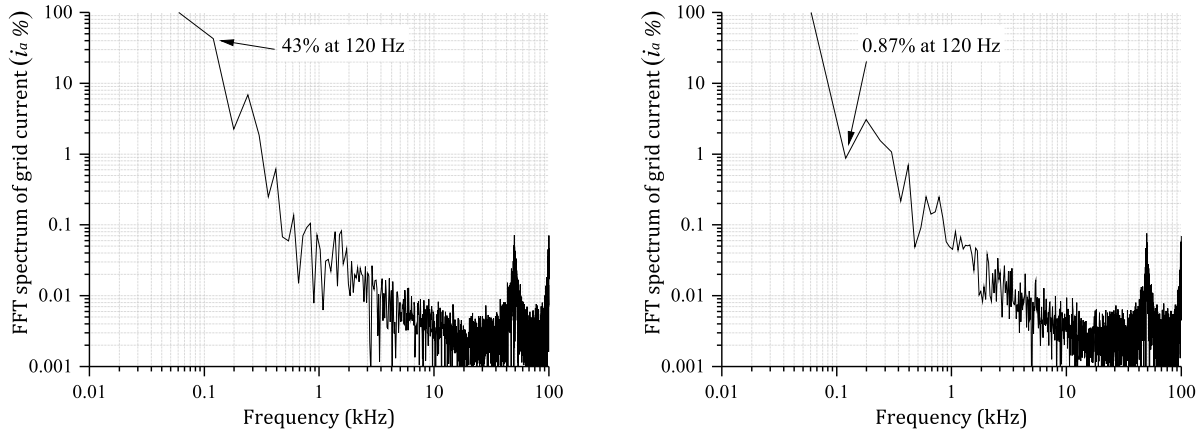


(a) Mode-1. (b) Mode-2.

**FIGURE 15.** Grid current FFT harmonic spectrum at 1.6 kW.

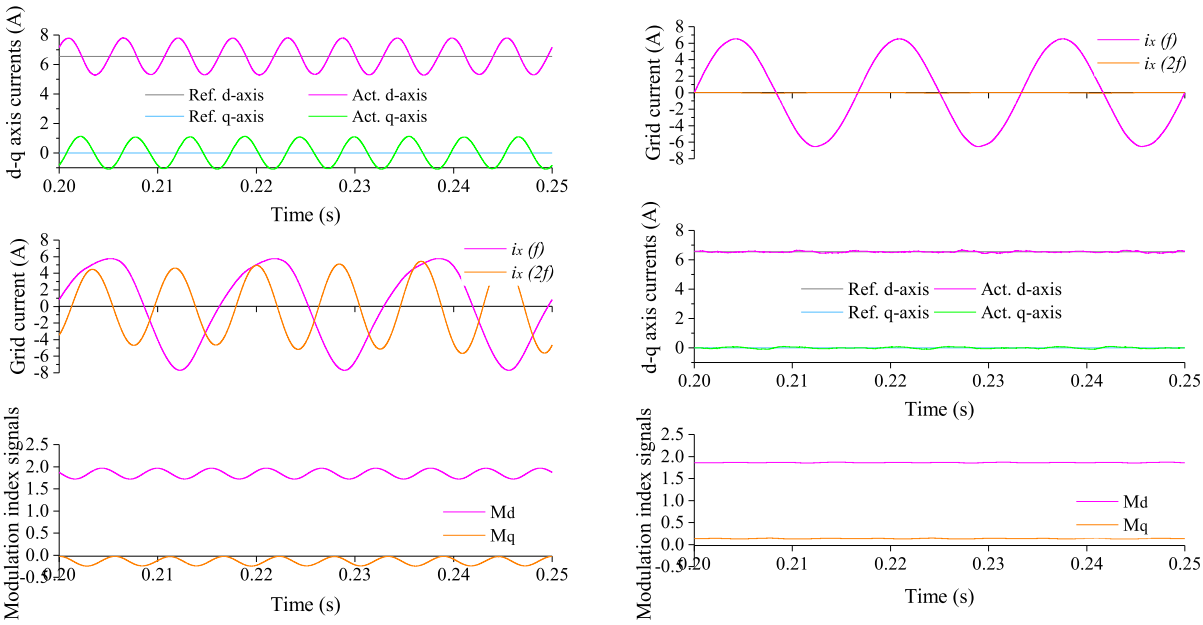


(a) Mode-1. (b) Mode-2.

**FIGURE 16.** TBFBI Control system signals under Mode-1 and Mode-2 at 1.6 kW.

of 0.8 kW. Both figures show the three-phase grid voltage and current waveforms, output voltages across capacitors, battery input voltage and its current, voltage across main-switch, main-switch and HFT currents, and voltage across synchronous-switch. At rated power flow of 1.6 kW, Fig. 14(a) and Fig. 14(b) depicts the experimental results of the TBFBI at Mode-1 and Mode-2, respectively. Additionally, all oscilloscope images shown in Fig. 13 and Fig. 14 have two zoomed regions; (i.e.; A and B), for high-frequency switched waveforms at low and high duty-cycles, respectively. It worth to mention that in each power flow, the synchronous-switch voltage stress at Mode-1 and Mode-2 is similar due to the RC snubber-circuit design rigidity and the HFT leakage inductance [40]. It, also, reflects the reasonable design of the flyback HFTs for high power operation; (i.e; 550 W). Obviously, experimental results at 0.8 kW and 1.6 kW power flow show that the proposed control technique successfully controlled the TBFBI to inject the reference power to the grid at unity power factor.

At rated power flow of 1.6 kW considering Mode-1, the three-phase grid currents include high NSHC of 43%, as depicted in the grid current FFT harmonic spectrum in Fig. 15(a). This distortion causes high third-order harmonic in DC input current; (i.e.; peak-to-peak DC ripple current of 5.2 A). Moreover, the NSHC increases the circulating power

**TABLE 4. Comparative study of the proposed three-phase single-stage TBFBI.**

| Ref. | V-gain | $N_L$<br>$N_C$ | $N_{SW}$<br>$N_D$ | HFI<br>CMV | Operation modularity | Rating (kW)<br>Efficiency (%) | PWM technique | Advantage<br>Drawback |
|---|---|---|---|---|---|---|---|---|
| [44] | Buck-Boost | 3<br>3 | 6<br>0 | No<br>NA | Yes | 1.4<br>NA | SPWM | - Reduced number of components with voltage boosting capability.<br>- High voltage stress and low power quality. |
| [45] | Boost | 3<br>3 | 6<br>0 | No<br>NA | Yes | 0.4<br>NA | CMS-PWM<br>DMS-PWM<br>SV-PWM | - Boosting inverter with reduced elements count and voltage boosting capability.<br>- High voltage stress. |
| [6] | CUK | 6<br>6 | 6<br>0 | No<br>NA | Yes | 2.5<br>NA | PR-PWM | - Voltage boosting capability and reduced stress.<br>- Increased passive element and inverter footprint. |
| [37] | CUK | 6<br>6 | 6<br>0 | Yes<br>Yes | Yes | 2.5<br>NA | PR-PWM | - Voltage boosting capability, reduced input ripple, and stress.<br>- Increased passive element and inverter footprint. |
| [38] | Buck-Boost | 0<br>2 | 27<br>0 | No<br>NA | No | NA<br>NA | SPWM | - ANPC-MLI with voltage boosting and enhanced power quality.<br>- Increased number of switches. |
| [39] | CUK | 6<br>6 | 6<br>0 | Yes<br>Yes | Yes | 0.5<br>91 | DMS-PWM | - Voltage boosting capability and reduced circulating power and voltage stress.<br>- Increased passive element, input ripples, and inverter footprint. |
| [33] | SEPIC | 3<br>7 | 6<br>0 | Yes<br>Yes | Yes | 1.6<br>86.5 | SPWM | - Improved two-loop controller for grid current regulation with NSHC.<br>- Requires large input electrolytic capacitor for input ripple minimization. Also, the inverter size is large considering the large size and number of passive elements that diminish inverter efficiency at rated power. |
| Proposed | Flyback | 1<br>4 | 6<br>0 | Yes<br>Yes | Yes | 1.6<br>89.93 | Single carrier SPWM | - Improved control scheme with NSHC compensation strategy, single-stage, and enhanced footprint.<br>- Requires more analysis for power loss distribution for efficiency enhancement. |

between the inverter modules, which increases reactive power component and diminishes the system power factor (0.918). On the other hand after considering NSHC compensation, the injected three-phase grid current is almost pure sinusoidal waveforms with low second-order harmonic component of 0.87%, which reduces the input DC peak-to-peak current ripple to 0.35 A, as shown in Fig. 15(b). The peak-to-peak current-ripple at the input DC-side is 0.35 A, which is 2.1% of the DC input current that matches the IEEE-1547 standards for DER applications. The control parameters of the proposed TBFBI at Mode-1 and Mode-2 are depicted in Fig. 16. For Mode-1, the grid-injected currents include high second-order harmonic, which causes third-order harmonic in the d-q axis currents as well as modulation index signals as shown in Fig. 16(a). For Mode-2, the d-q axis currents and modulation index signals follows the reference values with low ripples as depicted in Fig. 16(b). Fig. 17 shows WT1800 power analyzer measurements of the TBFBI system at Mode-1 considering nanocrystalline HF core, however, Fig. 18(a) and Fig. 18(b) shows the system results at Mode-2 considering nanocrystalline and soft ferrite cores, respectively. It is clear that in Mode-2, THD of the grid injected current reduced from 39.29% to 3.95% due to the elimination of the second-order harmonic-components, which matches IEEE and ICE harmonic standard limit. The analyzer images show the system overall efficiency which is 89.9% for Mode-1 and 88.09% for Mode-2. The reduction in system efficiency is due to the modification of the modulation

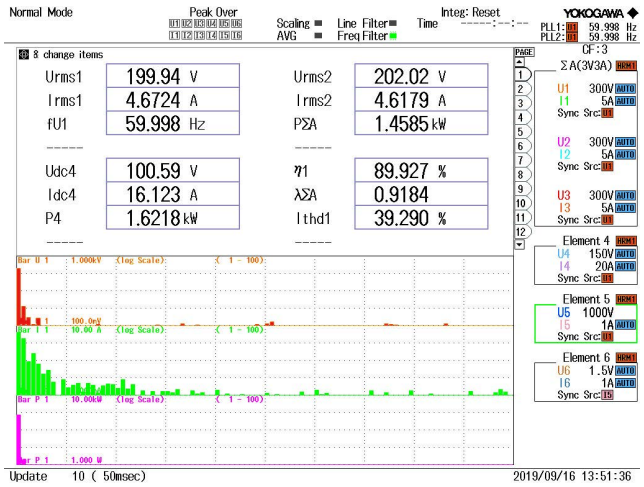


**FIGURE 17. Power analyzer measurements of the proposed TBFBI at 1.6 kW at Mode-1 considering nanocrystalline core.**

index that required more dc power to compensate the second order harmonic. Moreover, elimination of the second order harmonic increases the power factor at grid-side from 0.918 to 0.998 due to the reduction in reactive power. Also according to Fig. 18(a) and Fig. 18(b), THD of the grid injected current is 3.95% in case of using nanocrystalline core for the HFT of the TBFBI system which is less than the permissible limits of the IEEE standard. On the other hand, THD of the grid injected current in case of using ferrite core is 5.9%, which

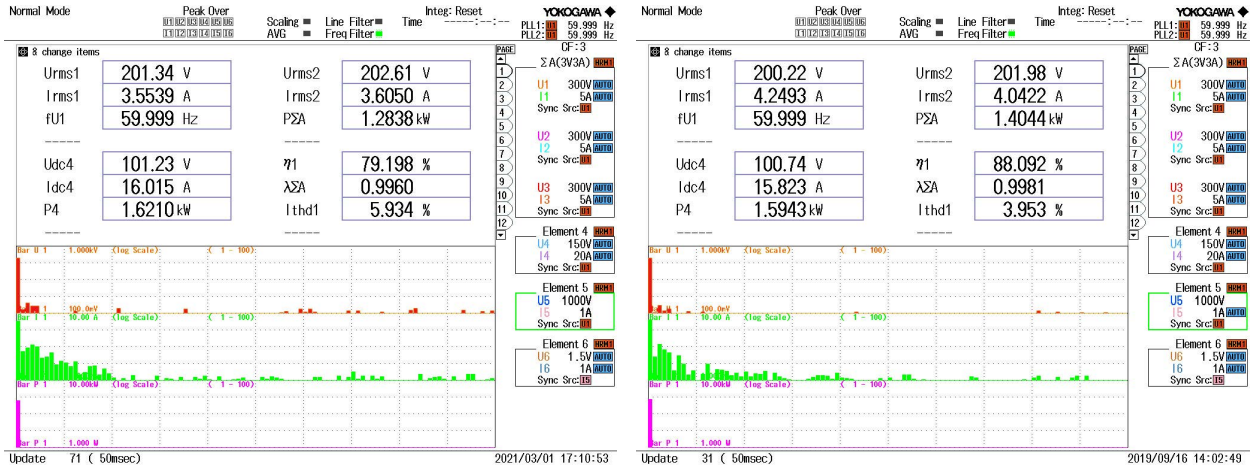


(a) EER soft-ferrite core. (b) nanocrystalline core.

**FIGURE 18.** Power analyzer measurements of the proposed TBFBI at 1.6 kW.

exceeds the permissible limits of the IEEE standard. It worth to mention that at 1 kW power flow the TBFBI efficiency is 90.88% and 90% before and after NSHC compensation, respectively.

In addition, efficiency profile of the proposed TBFBI is shown in Fig. 19 considering two magnetic cores (i.e.; nano-crystalline and EER soft-ferrite cores) for the HFT. For fair efficiency profile comparison between nano-crystalline and soft-ferrite cores. Obviously, the power loss of the TBFBI with nano-crystalline cores is less than that with soft ferrite materials. At 1.6 kW power flow, the system efficiency is 88.09% in case of nanocrystalline cores and 79.2% with soft ferrite cores. In addition, the power loss distributions over all components of the proposed TBFBI have been experimentally measured using Yokogawa WT1800 power analyser as depicted in Fig. 20.

In order to investigate the effectiveness of the control algorithm and its rigidity, the system performance has been tested considering a step change of the reference power flow. Fig. 21(a) and Fig. 21(b) show the TBFBI experimental results at mode-1 and Mode-2 during step changed from 0.4 kW to 1.6 kW in the reference power flow. In both cases, the actual and reference power agree well. The DC-input current and the injected grid current waveforms step from their related values at 0.4 kW to 1.6 kW without any overshoot considering very small settling time; (i.e.; 5 ms). It is clear that the input DC current includes a high third-order harmonic at Mode-1, whereas the controller eliminates this component from the DC current after considering the NSHC compensation at Mode-2.

In addition, the proposed three-phase TBFBI is compared with the recent topologies of single-stage inverters to illustrate its merits for industrial applications, as illustrated in Table 4. Clearly, the TBFBI utilized a reduced number of power switches, driver circuits, inductors, and capacitors compared with the other topologies for same rating and

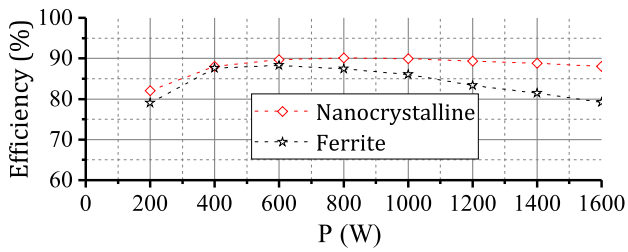


**FIGURE 19.** Experimental efficiency profile of the TBFBI considering nano-crystalline and soft ferrite cores.

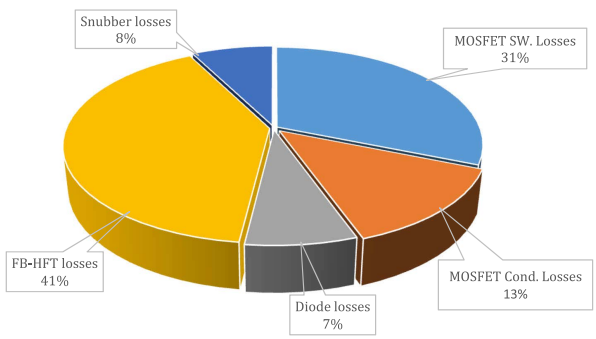


**FIGURE 20.** Power loss distribution of the proposed TBFBI.

application. In order to eliminate the common-mode leakage currents between the PV panel neutral-point and the ground of the AC network that causes many hazards and affect the system lifetime, small-size HFT based flyback converter modules are utilized [46], [47]. HFT provides galvanic isolation between the AC and DC sides that prevents leakage current injection and enhances system reliability in PV grid-tied applications. Moreover, it offers modularity operation feature with high-frequency isolation, which make it more flexible in PV applications. Also, differential based three-phase

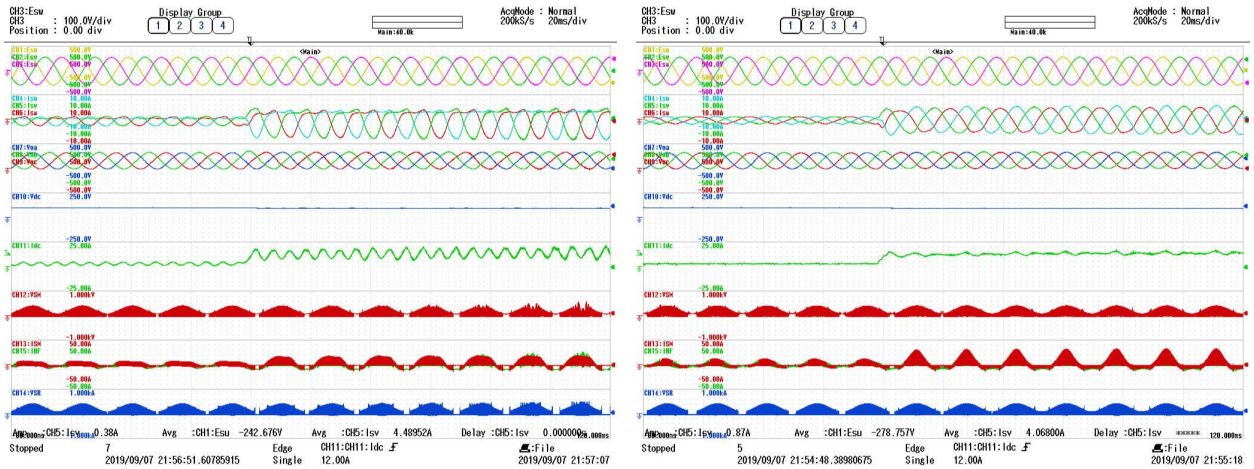

(a) Scope results for Mode-1.

(b) Scope results for Mode-2.

**FIGURE 21.** Experimental results of the TBFBI during step-changed grid injected power from 0.4 kW to 1.6 kW.

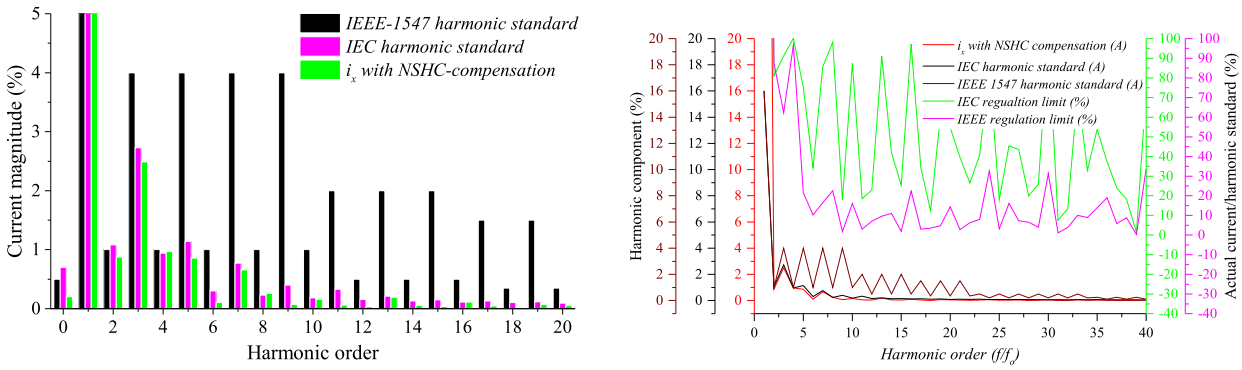


(a)

(b)

**FIGURE 22.** Grid-current harmonic orders in compared with IEC61000-3-2 and IEEE-1547 harmonic standards. (a) Bar chart of grid current harmonic orders. (b) Current harmonics vs IEC standards and regulation limits.

inverters usually offer a low operating efficiency compared with Dual-Active-Bridge based systems due to the existence of low-order harmonics and the voltage stress, which results from the voltage boosting property in a single-stage operation. According to previous literatures, average efficiency of differential-based three-phase inverters based on (Cuk, SEPIC,. . . .) is between (86-91%) [6], [33], [37]. On the other hand, grid-connected three-phase DC-AC inverters based on matrix or dual-active-bridge converters usually exhibit efficiency in the range of (94% to 97%) depending on the utilized switch type (i.e.; MOSFET, Sic or Gan) [48]. However, Matrix-based or DAB-based systems do not include voltage boosting property. Also, the necessary bulk electrolytic dc link capacitor in the DAB-based structures affects system reliability. In addition, both structures employs large number of power devices that increase system cost and footprint. It worth to mention that the proposed configuration is controlled via a two-loop control strategy considering only three current sensors and two voltage sensors to detect the grid current and voltage waveforms, which is less than the required sensors for similar inverter topologies presented in [37]. Also, comparison of the proposed inverter control technique with the recently published topologies based-on the number of control loops and required number of sensors are listed in Table 5.

Also, the grid-current harmonic orders of the TBFBI are compared with the IEC61000-3-2 (Class-A) and IEEE-1547 harmonic standards at rated power as depicted in Fig. 22. Fig. 22(a) shows comparison between low order harmonic components of the proposed system and permissible harmonic limits provided by IEC61000-3-2 (Class-A) and IEEE-1547 standards. On the other hand, Fig. 22(b) shows the harmonic regulation factor of the low order harmonic components, (i.e.; the percentage of TBFBI harmonic component over percentage of permissible limits provided by both standards). Obviously, the grid current DC component is 0.2%, which is less than the IEEE-1547 permissible limit (0.5%) as cleared in Fig. 22(a). In addition, all low order harmonic components (up to 2.4 kHz) of the TBFBI system is lower than the permissible limits provided by both standards as

**TABLE 5. Comparative study of the proposed single-stage TBFBI.**

| Control/Ref. | [23] | [37] | [34] | | [33] | Proposed |
|---|---|---|---|---|---|---|
| Modulation scheme | DMS | CMS | DMS | DMS & BCM | CMS | CMS |
| No. of stages | Single-stage | Single-stage | Two-stage | Two-stage | Single-stage | Single-stage |
| No. of loops | 5 | 3 | 1 | 2 | 2 (Current control only) | 2 (Current & voltage control) |
| Controller | PR | PR | NA | NA | PI | PI |
| F_{SW} (kHz) | 100 | 25 | 20 | 20 | 50 | 50 |
| THD (%) | 4 | 1.2 | Higher than 3.56 | 3.56 | 4.1 | 3.95 |
| No. of sensors | 7 | 7 | 4 | 4 | 5 (Current control only ) | 5 (Current & voltage control) |
| Power rating, W | 500 | 2500 | 100 | 100 | 1600 | 1600 |
| Switches rating | (GS66508P) 650 V, 30 A | (IRG7PH50K10D) 1200 V, 90 A | NA | NA | (C2M0040120D) 1200 V, 60 A | (C2M0040120D) 1200 V, 60 A |

shown in Fig. 22(a) and Fig. 22(b). Obviously, all values of regulation limits of the proposed TBFBI are less than 100% that match the grid standard requirements for grid-tied PV inverter applications.

## V. CONCLUSION

This paper has presented an isolated grid-tied TBFBI considering HFT for galvanic isolation and small passive elements compared with conventional three-phase inverters, which comparatively enhances the inverter power density and footprint. A new mathematical model of the proposed TBFBI has been presented, which confirms the existence of NSHC in the grid current waveforms. In addition, terminal voltage estimation strategy has been used to control the output voltage of each flyback module, which reduces the required number of sensors. Hence, the proposed control method uses the least number of control loops and required sensors compared with other three-phase differential converters topologies. Moreover, a simple compensation strategy for the NSHC via single-pole integrator has been utilized to improve THD of the grid-injected current waveforms. The second control-loop integrator enrich the main control-loop with the origin-pole, which boosts DC-gain of the proposed inverter that enhances the system accuracy and stability. Furthermore, the proposed second loop decreases the first control-loop order, which simplifies the computational algorithm and enhances the DSP execution time. HFT with nanocrystalline core is designed for compactness and loss aspects of the TBFBI. The proposed TBFBI is experimentally validated using a laboratory prototype based 200V and 1.6kW power flow for grid-tied application. Experimental results prove the accuracy of the control technique in injecting sinusoidal current waveforms to the grid at unity power factor in addition to the NSHC elimination providing grid-current THD of 3.95% and input DC current ripple of 2.1%, which follows the permissible limits of the IEEE-1547 and IEC61000-3-2 (Class-A) standards.

## ACKNOWLEDGMENT

This publication was made possible by research collaboration between South Valley University, Nagoya Institute of Technology, and Jazan University. The statements made herein are solely the responsibility of the authors. The Open Access funding is provided by the South Valley University, Qena, Egypt.

## REFERENCES

[1] B. Tamyurek and B. Kirimer, "An interleaved high-power flyback inverter for photovoltaic applications," *IEEE Trans. Power Electron.*, vol. 30, no. 6, pp. 3228–3241, Jun. 2015.

[2] N. Müller, H. Renaudineau, F. Flores-Bahamonde, S. Kouro, and P. Wheeler, "Ultracapacitor storage enabled global MPPT for photovoltaic central inverters," in *Proc. IEEE 26th Int. Symp. Ind. Electron. (ISIE)*, Jun. 2017, pp. 1046–1051.

[3] Z. Zhang, X.-F. He, and Y.-F. Liu, "An optimal control method for photovoltaic grid-tied-interleaved flyback microinverters to achieve high efficiency in wide load range," *IEEE Trans. Power Electron.*, vol. 28, no. 11, pp. 5074–5087, Nov. 2013.

[4] A. I. M. Ali, M. A. Sayed, and E. E. M. Mohamed, "Modified efficient perturb and observe maximum power point tracking technique for grid-tied PV system," *Int. J. Electr. Power Energy Syst.*, vol. 99, pp. 192–202, Jul. 2018.

[5] S. Kouro, J. I. Leon, D. Vinnikov, and L. G. Franquelo, "Grid-connected photovoltaic systems: An overview of recent research and emerging PV converter technology," *IEEE Ind. Electron. Mag.*, vol. 9, no. 1, pp. 47–61, Mar. 2015.

[6] A. Darwish, D. Holliday, S. Ahmed, A. M. Massoud, and B. W. Williams, "A single-stage three-phase inverter based on Cuk converters for PV applications," *IEEE J. Emerg. Sel. Topics Power Electron.*, vol. 2, no. 4, pp. 797–807, Dec. 2014.

[7] B. N. Alajmi, K. H. Ahmed, G. P. Adam, and B. W. Williams, "Single-phase single-stage transformer less grid-connected PV system," *IEEE Trans. Power Electron.*, vol. 28, no. 6, pp. 2664–2676, Jun. 2013.

[8] A. Darwish and M. A. Elgenedy, "Current-source modular medium-voltage grid-connected system with high-frequency isolation for photovoltaic applications," *IEEE Trans. Energy Convers.*, vol. 34, no. 1, pp. 255–266, Mar. 2019.

[9] T. A. Ahmed, E. E. M. Mohamed, A.-R. Youssef, A. A. Ibrahim, M. S. R. Saeed, and A. I. M. Ali, "Three phase modular multilevel inverter-based multi-terminal asymmetrical DC inputs for renewable energy applications," *Eng. Sci. Technol., Int. J.*, vol. 23, no. 4, pp. 831–839, Aug. 2020.

[10] P. Sun, C. Liu, J.-S. Lai, C.-L. Chen, and N. Kees, "Three-phase dual-buck inverter with unified pulsewidth modulation," *IEEE Trans. Power Electron.*, vol. 27, no. 3, pp. 1159–1167, Mar. 2012.

[11] R. S. Alishah, D. Nazarpour, S. H. Hosseini, and M. Sabahi, "Reduction of power electronic elements in multilevel converters using a new cascade structure," *IEEE Trans. Ind. Electron.*, vol. 62, no. 1, pp. 256–269, Jan. 2015.

[12] L. Zhang, M. J. Waite, and B. Chong, "Three-phase four-leg flying-capacitor multi-level inverter-based active power filter for unbalanced current operation," *IET Power Electron.*, vol. 6, no. 1, pp. 153–163, Jan. 2013.

[13] A. I. M. Ali, M. A. Sayed, T. Takeshita, A. M. M. Hassan, and A. M. Azmy, "A single-phase modular multilevel inverter based on controlled DC-cells under two SPWM techniques for renewable energy applications," *Int. Trans. Electr. Energy Syst.*, vol. 31, no. 1, Jan. 2021, Art. no. e12599.

[14] F. Gao, R. Teodorescu, F. Blaabjerg, P. C. Loh, and D. M. Vilathgamuwa, "Topological design and modulation strategy for buck-boost three-level inverters," *IEEE Trans. Power Electron.*, vol. 24, no. 7, pp. 1722–1732, Jul. 2009.

[15] T. K. S. Freddy, N. A. Rahim, W.-P. Hew, and H. S. Che, "Modulation techniques to reduce leakage current in three-phase transformerless H7 photovoltaic inverter," *IEEE Trans. Ind. Electron.*, vol. 62, no. 1, pp. 322–331, Jan. 2015.

[16] M. A. Rezaei, K.-J. Lee, and A. Q. Huang, "A high-efficiency flyback micro-inverter with a new adaptive snubber for photovoltaic applications," *IEEE Trans. Power Electron.*, vol. 31, no. 1, pp. 318–327, Jan. 2016.

[17] J. A. Pomilio and G. Spiazzi, "High-precision current source using low-loss, single-switch, three-phase AC/DC converter," *IEEE Trans. Power Electron.*, vol. 11, no. 4, pp. 561–566, Jul. 1996.

[18] V. Chunkag, "Parallelling three-phase AC to DC converter using CUK rectifier modules based on power balance control technique," *IET Power Electron.*, vol. 3, pp. 511–524, Jul. 2010.

[19] R. Davoodnezhad, D. G. Holmes, and B. P. McGrath, "A novel three-level hysteresis current regulation strategy for three-phase three-level inverters," *IEEE Trans. Power Electron.*, vol. 29, no. 11, pp. 6100–6109, Nov. 2014.

[20] M. S. Diab, A. Elserougi, A. M. Massoud, A. S. Abdel-Khalik, and S. Ahmed, "A four-switch three-phase SEPIC-based inverter," *IEEE Trans. Power Electron.*, vol. 30, no. 9, pp. 4891–4905, Sep. 2015.

[21] A. I. M. Ali, M. A. Sayed, and T. Takeshita, "Isolated single-phase single-stage DC-AC cascaded transformer-based multilevel inverter for stand-alone and grid-tied applications," *Int. J. Electr. Power Energy Syst.*, vol. 125, Feb. 2021, Art. no. 106534.

[22] R. O. Caceres and I. Barbi, "A boost DC-AC converter: Analysis, design, and experimentation," *IEEE Trans. Power Electron.*, vol. 14, no. 1, pp. 134–141, Jan. 1999.

[23] A. Kulkarni, A. Gupta, and S. K. Mazumder, "Resolving practical design issues in a single-phase grid-connected GaN-FET-Based differential-mode inverter," *IEEE Trans. Power Electron.*, vol. 33, no. 5, pp. 3734–3751, May 2018.

[24] J. Ebrahimi, E. Babaei, and G. B. Gharehpetian, "A new topology of cascaded multilevel converters with reduced number of components for high-voltage applications," *IEEE Trans. Power Electron.*, vol. 26, no. 11, pp. 3109–3118, Nov. 2011.

[25] D. Chen and G. Wang, "Differential buck DC–DC chopper mode inverters with high-frequency link," *IEEE Trans. Power Electron.*, vol. 26, no. 5, pp. 1444–1451, May 2011.

[26] G. V. Silva, J. M. de Andrade, R. F. Coelho, and T. B. Lazzarin, "Switched-capacitor differential boost inverter: Design, modeling, and control," *IEEE Trans. Ind. Electron.*, vol. 67, no. 7, pp. 5421–5431, Jul. 2020.

[27] G. Arunkumar, D. C. S. Padmanaban, B. R. Prusty, and B. Khan, "Implementation of optimization-based PI controller tuning for non-ideal differential boost inverter," *IEEE Access*, vol. 9, pp. 58677–58688, 2021.

[28] S. M. Babu, V. K. S. Veeramallu, B. L. Narasimharaju, A. K. Rathore, and H. S. Krishnamoorthy, "Novel non-isolated differential buck-boost inverter with single-stage conversion and reduced device voltage stress," in *Proc. IEEE Int. Conf. Power Electron., Smart Grid Renew. Energy (PESGRE)*, Jan. 2020, pp. 1–5.

[29] D. Lyu, Y. Sun, C. A. Teixeira, Z. Ji, J. Zhao, and Q. Wang, "A modular multilevel dual buck inverter with adjustable discontinuous modulation," *IEEE Access*, vol. 8, pp. 31693–31709, 2020.

[30] J. Knight, S. A. Shirsavar, and W. Holderbaum, "An improved reliability Cuk based solar inverter with sliding mode control," *IEEE Trans. Power Electron.*, vol. 21, no. 4, pp. 1107–1115, Jul. 2006.

[31] A. I. M. Ali, M. A. Sayed, A. Shawky, and T. Takeshita, "Efficient single-stage three-phase isolated differential-based flyback inverter with selective harmonic compensation strategy for grid-tied applications," in *Proc. IEEE Appl. Power Electron. Conf. Expo. (APEC)*, Mar. 2020, pp. 1778–1785.

[32] A. I. M. Ali, T. Takeshita, and M. A. Sayed, "Three-phase PWM inverter for isolated grid-connected renewable energy applications," *Energies*, vol. 14, no. 12, p. 3701, Jun. 2021.

[33] A. Shawky, T. Takeshita, M. A. Sayed, M. Aly, and E. M. Ahmed, "Improved controller and design method for grid-connected three-phase differential SEPIC inverter," *IEEE Access*, vol. 9, pp. 58689–58705, 2021.

[34] T. Lodh, N. Pragallapati, and V. Agarwal, "Novel control scheme for an interleaved flyback converter based solar PV microinverter to achieve high efficiency," *IEEE Trans. Ind. Appl.*, vol. 54, no. 4, pp. 3473–3482, Jul. 2018.

[35] H. Kim, J. S. Lee, and M. Kim, "Downsampled iterative learning controller for flyback CCM inverter," *IEEE Trans. Ind. Electron.*, vol. 65, no. 1, pp. 510–520, Jan. 2018.

[36] A. B. Shitole, S. Sathyan, H. M. Suryawanshi, G. G. Talapur, and P. Chaturvedi, "Soft-switched high voltage gain boost-integrated flyback converter interfaced single-phase grid-tied inverter for SPV integration," *IEEE Trans. Ind. Appl.*, vol. 54, no. 1, pp. 482–493, Jan. 2018.

[37] A. Darwish, A. M. Massoud, D. Holliday, S. Ahmed, and B. W. Williams, "Single-stage three-phase differential-mode buck-boost inverters with continuous input current for PV applications," *IEEE Trans. Power Electron.*, vol. 31, no. 12, pp. 8218–8236, Dec. 2016.

[38] J. Zeng, W. Lin, and J. Liu, "Switched-capacitor-based active-neutral-point-clamped seven-level inverter with natural balance and boost ability," *IEEE Access*, vol. 7, pp. 126889–126896, 2019.

[39] S. Mehrnami, S. K. Mazumder, and H. Soni, "Modulation scheme for three-phase differential-mode Ćuk inverter," *IEEE Trans. Power Electron.*, vol. 31, no. 3, pp. 2654–2668, Mar. 2016.

[40] R. W. Erickson and D. Maksimovic, *Fundamentals of Power Electronics*. Springer, 2007.

[41] G. M. L. Chu, D. D. C. Lu, and V. G. Agelidis, "Practical application of valley current mode control in a flyback converter with a large duty cycle," *IET Power Electron.*, vol. 5, no. 5, pp. 552–560, May 2012.

[42] S. Lee, "Demystifying type II and type III compensators using op-amp and OTA for DC-DC converters," Texas Instrum., Appl. Rep. SLVA662, Jul. 2014.

[43] N. Rana, A. Ghosh, and S. Banerjee, "Development of an improved tristate buck–boost converter with optimized Type-3 controller," *IEEE J. Emerg. Sel. Topics Power Electron.*, vol. 6, no. 1, pp. 400–415, Mar. 2018.

[44] C. Cecati, A. Dell'Aquila, and M. Liserre, "A novel three-phase single-stage distributed power inverter," *IEEE Trans. Power Electron.*, vol. 19, no. 5, pp. 1226–1233, Sep. 2004.

[45] M. S. Diab, A. Elserougi, A. S. Abdel-Khalik, A. M. Massoud, and S. Ahmed, "Modified modulation scheme for photovoltaic fed grid-connected three-phase boost inverter," in *Proc. 39th Annu. Conf. IEEE Ind. Electron. Soc. (IECON)*, Nov. 2013, pp. 1735–1740.

[46] A. Darwish, S. Alotaibi, and M. A. Elgenedy, "Current-source single-phase module integrated inverters for PV grid-connected applications," *IEEE Access*, vol. 8, pp. 53082–53096, 2020.

[47] B. W. Williams, "Generation and analysis of canonical switching cell DC-to-DC converters," *IEEE Trans. Ind. Electron.*, vol. 61, no. 1, pp. 329–346, Jan. 2014.

[48] E. Gurpinar and A. Castellazzi, "Single-phase T-type inverter performance benchmark using Si IGBTs, SiC MOSFETs, and GaN HEMTs," *IEEE Trans. Power Electron.*, vol. 31, no. 10, pp. 7148–7160, Oct. 2016.

**AHMED ISMAIL M. ALI** (Student Member, IEEE) was born in Qena, Egypt, in 1991. He received the B.Sc. and M.Sc. degrees in electrical engineering from the Faculty of Engineering and Technology, South Valley University, Qena, in 2013 and 2017, respectively. In 2018, he joined the Nagoya institute of Technology, Nagoya, Japan, as the Ph.D. Student. Since 2013, he has been an Administrator with the Department of Electrical Engineering, Faculty of Engineering, South Valley University, and a Research Assistant since 2017, where he is currently an Assistant Lecturer. He has coauthored number of publications including single-three phase PWM dc/ac multilevel inverters, dc/dc converters, isolated MMxC, and advanced MPPT techniques for PVs and WECSs. His research interests include power electronic converters, PWM techniques dc/ac and ac/dc converters, modular multilevel converters (MMxC), control systems, renewable energy applications, and battery chargers for electric vehicle applications. He joined the IEEE Power Electronics and Industry Application Societies.

**MAHMOUD A. SAYED** (Senior Member, IEEE) was born in Qena, Egypt, in 1974. He received the B.Sc. and M.Sc. degrees in electrical engineering from Minia University, Minya, Egypt, in 1997 and 2001, respectively, and the Ph.D. degree in electrical engineering from the Nagoya Institute of Technology, Nagoya, Japan, in 2010. Since 1999, he has been an Assistant Lecturer with the Department of Electrical Engineering, Faculty of Energy Engineering, Aswan University, Aswan, Egypt, and a Lecturer since 2001. Since 2010, he has been an Assistant Professor with the Faculty of Engineering, South Valley University, Qena, where he was an Associate Professor, from 2015 to 2020. He is currently a Full Professor with the Faculty of Engineering, South Valley University. His research interests include wireless power transfer for industrial applications and electric vehicles, voltage regulation and loss minimization of electrical distribution systems using series and shunt power converters, pulse width modulation (PWM) techniques for bidirectional ac/dc and direct ac/ac converters, modular multilevel converters (MMxC), single and three-phase multilevel inverters, battery charger, power regeneration techniques for electric vehicles, and renewable energy applications and machine drives. Dr. Sayed is a senior member of the IEEE Power Electronics and Industry Application Societies.

**TAKAHARU TAKESHITA** (Senior Member, IEEE) was born in Aichi, Japan, on August 1959. He received the B.S. and M.S. degrees in electrical engineering from the Nagoya Institute of Technology, Nagoya, Japan, in 1982 and 1984, respectively, and the Ph.D. degree from Nagoya University, Nagoya, in 1990. Since 1991, he has been with the Nagoya Institute of Technology, where he is currently a Full Professor. He is engaged in research on power converters and motor drives. He is a member of the Society of Instrument and Control Engineers (SICE), the Society of Signal Processing Applications and Technology of Japan (SSPATJ), and the Institute of Electrical and Electronic Engineering (IEEE).

**ZUHAIR MUHAMMED ALAAS** (Member, IEEE) received the B.S. degree from the King Fahd University of Petroleum and Minerals (KFUPM), Dhahran, Saudi Arabia, in 2002, the M.S. degree from the University of Newcastle upon Tyne, Newcastle, U.K. in 2007, and the Ph.D. degree from Wayne State University, Detroit, Michigan, USA, in 2017, all in electrical engineering. From September 2002 to November 2010, he worked as a Lecturer with the Abha College, Technical and Vocational Training Corporation, Saudi Arabia. From November 2010 to June 2011, he worked as a Power Transmission Engineer with Saudi Electric Company. Since June 2011, he has been with Jazan University, where he is currently an Assistant Professor and the Department of Electrical Engineering Chairperson. His current research interests include energy storage devices, power electronics, microgrids, alternative/hybrid energy power generation systems, and motor drives.